Materials and Design 88 (2015) 1353–1365

Contents lists available at ScienceDirect

Materials and Design

journal homepage: www.elsevier.com/locate/jmad

Local corrosion behaviour of hybrid laser-MIG welded Al–Zn–Mg alloy joints

Shaohua Yan [a,1], Hui Chen [b,*,1], Chuanping Ma [b], Yuan Nie [b], Xiaomin Wang [c], Qing H. Qin [a]

[a] Research School of Engineering, Australia National University, Acton, ACT 2601, Australia
[b] School of Materials Science and Engineering, Southwest Jiaotong University, Chengdu, Sichuan 610031, China
[c] School of Life Science and Engineering, Southwest Jiaotong University, Chengdu, Sichuan 610031, China

ARTICLE INFO

Article history:
Received 6 May 2015
Received in revised form 9 July 2015
Accepted 27 August 2015
Available online 2 September 2015

Keywords:
Aluminium alloys
Hybrid laser-MIG welding
SCC

ABSTRACT

The local corrosion behaviour of a hybrid laser-metal-inert-gas (MIG) welded Al–Zn–Mg alloy joint is studied using pre-cracked bending samples immersed in 3.5% NaCl solution. To gain insight into the SCC susceptibility in different zones including the base metal (BM), heat affected zone (HAZ) and fusion zone (FZ), the corrosion surface, fractured surface and SCC propagation are investigated experimentally. The results illustrate that the BM in natural ageing (NA) state is more prone to induce SCC than the HAZ, a finding that differs from previous reports that the HAZ is more prone to induce SCC. The reason is explained via the welding process and corrosion method. Influence of post-weld heat treatment (PWHT) on SCC resistance of the hybrid laser-MIG Al–Zn–Mg joint is examined as well. The results show that the resistance of the welded joint to SCC can be enhanced by PWHT. The microstructure change due to PWHT is shown to be responsible for this improvement.

1. Introduction

MIG/TIG welding is still being widely utilized to join Al–Zn–Mg alloys, although these welding processes have many drawbacks such as slow welding speed [1], wide HAZ and softening behaviour of FZ and HAZ [2,3]. For the sake of overcoming or minimizing these problems, laser arc hybrid welding was introduced [4], whose process advantages of laser welding and arc welding while compensating their weakness. Extensive studies have been carried out from aspects of optimizing welding parameters [5,6], studying formation of porosity [7], and controlling of the microstructure and mechanical properties of the welding product [8].

A particular phenomenon of fusion welding is that, cast microstructures and defects (i.e. porosity) exist in the FZ and partial recrystallization and grain growth occur in the HAZ of a weldment. As a result, the welded joint contains various microstructural and compositional heterogeneities. These heterogeneous microstructures plus residual tensile stress can lead to stress corrosion cracking (SCC), especially for a welded Al–Zn–Mg alloys joint, whose base metal is prone to SCC. As a result, the corrosion behaviour of such welded joint has received significant attention from researchers. Kelsey [9] reported that an increase in heat input resulted in increasing susceptibility to SCC, and this corrosion behaviour could be improved by post-weld ageing. Reboul and Lashermes [10] conducted the study of influence of filler materials and PWHT on the corrosion behaviour of a welded lap joint of AA7020. They showed that filler material ER5356 was more resistant to SCC than filler material ER5039 was. They also reported that different PWHTs may change the SCC susceptibility of the welded joint. Wu and Wang [11] also found that corrosion resistance of MIG welded AA7005 joints could be changed with different filling materials and PWHTs.

The literature review above shows: (1) SCC resistance of the welded joint can be enhanced either by changing filler materials or PWHTs. The former is limited to the fusion zone while the latter can be effective for the whole joint. Ageing can lead to changes in (i) size, area fraction, and composition of GBPs; (ii) solute segregation to grain boundaries; (iii) precipitate free zone (PFZ) width and solute concentration profiles across PFZs; and (iv) matrix precipitate (MPt) size and coherency (slip mode). As these changes happen simultaneously during ageing, the relative importance of these factors is very difficult to establish [12,13]. (2) Although SCC behaviour of TIG/MIG/EB welded joints of 7xxx serials alloys has been well studied, research into the corrosion behaviour of laser-MIG welded Al–Zn–Mg joints is still lacking. It should be noted that the resistance of welded structure might be altered by the welding process. Fahimpour et al. [14] indicated that the corrosion resistance of AA6061 joints fabricated by FSW was superior to that of gas tungsten arc welding (GTAW) joints. Hu et al. [15] showed that plasma welded 2xxx series aluminium alloy joints had superior SCC resistance comparing to FSW welded joints. Besides, in the real loading circumstance, the stress might be concentrated in a certain zone (i.e., HAZ); in such case, the local SCC resistance of the welded joint is critical. However, no published research exists into the local SCC behaviours of welded Al–Zn–Mg joints.

* Corresponding author.
E-mail addresses: shaohua.yan@anu.edu.au (S. Yan), xnrpt@163.com (H. Chen), qinghua.qin@anu.edu.au (Q.H. Qin).
[1] These authors made equal contribution to this paper.

http://dx.doi.org/10.1016/j.matdes.2015.08.140
0264-1275/

Table 1
Chemical composition of BM and filler material (wt.%).

	Si	Fe	Cu	Mg	Cr	Zn	V	Mn	Zr	Al
A7N01	0.10	0.13	0.05	1.15	0.19	4.18	0.05	0.40	0.12	Balance
ER5356	0.10	0.40	0.10	4.80	0.10	0.10	–	0.15	–	Balance

In this paper, the corrosion characteristics of hybrid laser-MIG welded Al–Zn–Mg joints are investigated via stress corrosion tests in the BM, HAZ and FZ, using pre-cracked bending samples bathed in 3.5% NaCl solution. Furthermore, the influence of PWHT on corrosion behaviour is studied. The influence of PWHT on the strength of the joint is also briefly studied. The results are analysed on the basis of the mechanisms of anodic dissolution and HIC. The aim of this paper is to obtain information about the local SCC behaviour of hybrid laser-MIG welded Al–Zn–Mg alloy joints. The work is important for broadening the application of hybrid laser-MIG welding in the joining of Al–Zn–Mg alloys.

2. Materials and methods

2.1. Materials and welding method

The material was A7N01P-T4 plates, which was industrial solution treated first and then naturally aged at room temperature. Hybrid laser-MIG welding process was utilized to join these plates. The filler material was ER5356 with the diameter of 1.6 mm. The chemical compositions of base metal (A7N01 P-T4) and filler material are shown in Table 1. Details about hybrid laser-MIG welding system can be found elsewhere [2]. After a numerous experiments, the suitable parameters were as follows: $P_{laser} = 1.3$ kW, $I_{MIG} = 130$ A, $U_{MIG} = 21.7$ V, and $v = 0.83$ m/min.

2.2. Post-weld heat treatment

With the aim of investigating the effect of PWHT on the microstructure and corrosion behaviour of the welded joints, each welded sample was treated by one of the heat treatments listed in Table 2.

2.3. Microstructure examination and mechanical test

The samples used for microstructure analyses were first abraded with 600#, 800#, 1000# and 1500# grit abrasive papers and finally polished. Then the polished samples were etched by Keller's etch, and the microstructure was investigated using an AX10 ZEISS Optical Microscope (OM). To get the distribution of the precipitates of the fusion zone, another samples was polished with collision silicon suspension, and then observed using FEI Helios 600 Nanolab Focus Ion Beam system, the composition of the precipitates were analysed using EDAX. Thin foils for transmission electron microscope (TEM) observation were first ground to below 30 μm using abrasive papers, then thinned by a Model 691 Precision Ion Polishing System (PIPS™), and observed on a Jeol JEM 2010 TEM.

2.4. Microhardness and tensile test

Microhardness tests were conducted across the welds using a Vickers hardness tester with a load of 3000 g and a dwell time of 15 s. The position of microhardness was in the middle of the specimen, which was 2 mm away from the upper surface. Tensile test was performed according to the ASTM B557-10 standard [16]. The dimensions of a tensile test sample are shown in Fig. 1. The tensile test result was the average of three samples. These values were used to calculate the external applied stress in the SCC test.

Table 2
Process parameters for post-welding heat treatment.

Condition	Heat treatment
NA	Natural ageing for 30 days
T6	Aged at 120 °C for 24 h, then water quenched
T73	First aged at 110 °C for 8 h, then 177 °C for 8 h, and then water quenched

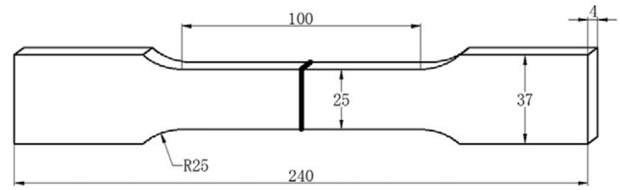

Fig. 1. Dimensions of tensile test sample (all in mm).

2.5. Stress corrosion test

The stress corrosion test followed the standard of GB 15970.6-2007 [17]. A pre-cracked specimen was used for three-point bending tests under constant displacement. The specimen was cut to make a notch with a length of 2 mm using electrical discharge machining (EDM), and then pre-cracked with a crack length of 0.45–0.55 W (W stands for the width of the sample). All pre-cracked specimens were ground using 1500# abrasive papers to obtain the same surface. The stress applied to the hybrid laser-MIG welded joint was calculated according to the equation:

$$\sigma = \frac{6Ety}{h^2} \tag{1}$$

where E is the elastic modulus (71.0 GPa), t is the thickness of the specimen, y is the height of deflection and h is the distance between inner supports. The stress (σ) used in this study was the yield stress calculated from the tensile test results.

To simulate actual corrosion conditions such as sunshine, wind and moisture, the corrosion test was conducted in a corrosion testing cell, shown in Fig. 2. The samples were immersed in 3.5% NaCl solution for 15 min, and then exposed in the atmosphere in the cell for 50 min before being immersed in 3.5% NaCl solution again.

The surface of each sample was observed after being immersed for 5 days and 20 days, respectively. After 20 days, the sample was bent until fracture to observe the fractured surface using OM and SEM. The crack length was measured according to GB 15970.6-2007.

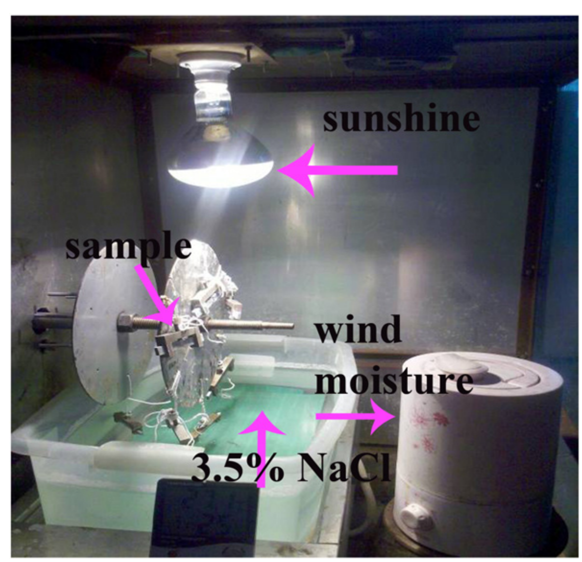

Fig. 2. Cell for stress corrosion cracking testing.

3. Results

3.1. Microstructure

Fig. 3 shows the microstructure of the centre of FZ after PWHT in NA, T6 and T73, respectively. Fine dendritic microstructure and precipitates are found in the FZ in NA (Fig. 3(d)), where the grain size is relatively small. However, after PWHT, the grain size is enlarged to about 200 μm and 300 μm in T6 and T73, respectively. It can be seen from Fig. 3(e)–(f) that some grains consist of large dendritic crystals. Compared to the FZ in NA, the FZs in T6 and T73 temper also contain a small amount of larger precipitates. To study the composition of these phases in fusion zone, SEM observation was made, results shown in Fig. 4. Round-like elongated phases can be found for all of these three tempers. According to the EDX results, some phases consists of Al, Mg and Zn, while some also containing Fe and Mn. For the fusion zone made of 5xxx serials filling materials, η ($MgZn_2$) and T (Al_2Mg_3Zn) is the main strengthening phase, but some other elements can also be seen in dispersed second intermetallic phases. Another finding from the SEM images is that the number of precipitation is affected by PWHT. The amount of phases in the NA and T73 is larger than that in T6. The precipitates probably experienced dissolution and coarsening in T6, and re-precipitation in T73.

The microstructure of HAZ after different PWHTs is shown in Fig. 5. The view point was positioned about 4 mm away from the weld centre. Comparing Fig. 5(a) and (b), no distinct difference can be observed between as-weld and NA conditions in this observation scale. In NA condition (Fig. 5(b)), two distinct regions can be seen because of the non-isothermal history during welding. One region is the reverted zone; the other is the transition zone. In the reverted zone, the large precipitates both along the GB and within the grain are distributed discontinuously, indicating that the microstructure is inhomogeneous. Among the grains, some have precipitates of various sizes whereas others have no precipitates (shown as clear space) due to dissolution during welding. In the transition zone, the distribution of the precipitates along the GB is also discontinuous, but their size is much smaller. Compared with the precipitation in NA, the HAZ in T6 results in three changes (see Fig. 5(c)): (1) the GB is thinner than that in NA (Fig. 5(b)); (2) clear zones are found close to the GB; and (3) many more fine precipitates are found within the grain. All these changes indicate that the precipitates along the GB experienced dissolution during the PWHT, while precipitation occurred inside the grain. The microstructure of HAZ under T73 is shown in Fig. 5(d). Compared to T6, the notable change is that the density of precipitates reduces for precipitates distributed continuously along the GB.

Fig. 6 illustrates the microstructure of the BM after PWHT. No significant changes of grain size can be observed in the SEM images. Compared to FZ, PWHT had little influence on the grain size of BM and HAZ. This is due to the thermal history in different zones. For FZ, it experienced higher temperature than that of solution treatment, but BM and some part of HAZ had the lower temperature than that of the solution treatment. More details of the change in the BM due to PWHT can be seen in the TEM images shown in Fig. 17.

3.2. Microhardness and tensile properties

The profile of microhardness of the joint is shown in Fig. 7. The microhardness in as-weld condition is added to study the influence of PWHT on the mechanical properties of the welded joint. Inhomogeneity is observed in the hybrid laser-MIG welded joint under NA and as-weld condition. The order of microhardness in both NA and as-weld condition is: BM > HAZ > FZ. The average microhardness of as-weld FZ and HAZ is ~65 HV and 97 HV, respectively. After 30-days natural ageing, average microhardness in FZ and HAZ increases to ~70 HV and 105 HV, respectively. In spite of improvement of microhardness due to recovery of ageing at room temperature, softening behaviour can still be observed in FZ and HAZ. Softening behaviour can be observed in HAZ, where the microhardness increases with the distance from the fusion line, ranging from ~85 HV to ~103 HV. The softening behaviour of welded joint has also been observed by other researchers [3,18]. The reduced strength in FZ is due to the evaporation of strengthening alloying elements during welding [3], while the softening and variation of microhardness in HAZ is due to the dissolution and coarsening of strengthening precipitates [18].

After T6, the microhardness is more homogeneous, and the difference in microhardness among these three zones is minimal. The most dramatic change occurs in the BM as its microhardness decreases from 105 HV to 77 HV. T6 treatment seems to have little influence on the microhardness of the FZ, which is ~77 HV in this temper. However, FZ is considerably affected by the T73 heat treatment, in which the microhardness decreases to ~65 HV. The microhardness of the HAZ and BM reduces progressively to ~65 HV. The reason for the dramatically reduced microhardness of BM after T73 will be discussed in Section 4.1.

Fig. 8 illustrates the ultimate tensile strength (UTS) and yield strength of the welded joint and BM under as-weld and PWHT condition. Showing the same trends as the microhardness, the UTS of the BM is reduced drastically, decreasing from 430 MPa in NA to 393 MPa in T6 and 284 MPa in T73. The yield strength of the BM evidences a similar change, reducing from 301 MPa in NA to 220 MPa in T6 and 180.76 MPa in T73. The UTS and yield strength of the as-weld joint is 254.3 MPa and 180.5 MPa, respectively. After PWHT, NA increases the UTS and yield strength to 287 MPa and 207 MPa, and T6 almost does not have an influence of the UTS and yield strength, while T73 reduces the UTS and yield strength to 240 and 137 MPa. All of the tensile samples in these three conditions fracture in the fusion zone.

3.3. Stress corrosion test result

3.3.1. Macrograph of welded joint after SCC

The surface of each sample was examined after 5 day and 20 day dipping in 3.5% NaCl solution, respectively. The surface change of the BM in the different heat treatments is shown in Fig. 9. The surface smoothness of all samples deteriorates with increasing duration of corrosion. After 5 day immersion some blisters appear on the surface of the BM in NA but no such blisters are observed on the surface of other two tempers. After 20 days, blisters are found in the BM in all three tempers, but the surface layer of the BM at NA peels most severely whereas only a small proportion of blisters are found in T73 temper. The blisters are generated due to exfoliation corrosion and possibly the effect of hydrogen [19]. Comparison of the corrosion morphologies of the three kinds of sample shows that the BM at NA temper is most susceptible to corrosion attack and T73 has stronger corrosion resistance than the other samples. We can see that, from the macrographs of BM, PWHTs could make the corrosion resistance of Al–Zn–Mg alloys better.

As shown in Fig. 10, samples in the HAZ experienced the same trend as that in BM: the surface smoothness deteriorates with increasing duration of immersion. However, the corrosion resistance for samples in the HAZ differs at different tempers. Due to the corrosion attack, the surface is peeled and the rolling direction can be seen in the HAZ in NA temper, whereas the appearance just darkens for T6 and T73. As illustrated in Fig. 11, although the surfaces of the BM and the HAZ in these three tempers are attacked by corrosion, the appearances of the samples in the FZ in all tempers do not change. The surprising result is that with the increase in duration of the surface of the FZ brightens. The corrosion potential of the HAZ is greater than that of the FZ, which causes galvanic corrosion. The electropotential of 5xxx serials Al and 7xxx serials Al is −0.85 V and −0.96 V, respectively. Thus, there is galvanic corrosion happening between these two zones with HAZ acting as anodic member while FZ as cathodic member. That means the HAZ is dissolved while the FZ is protected. Over time, the HAZ darkens due to corrosion while the FZ is relatively brighter Therefore, the surface of FZ brightens.

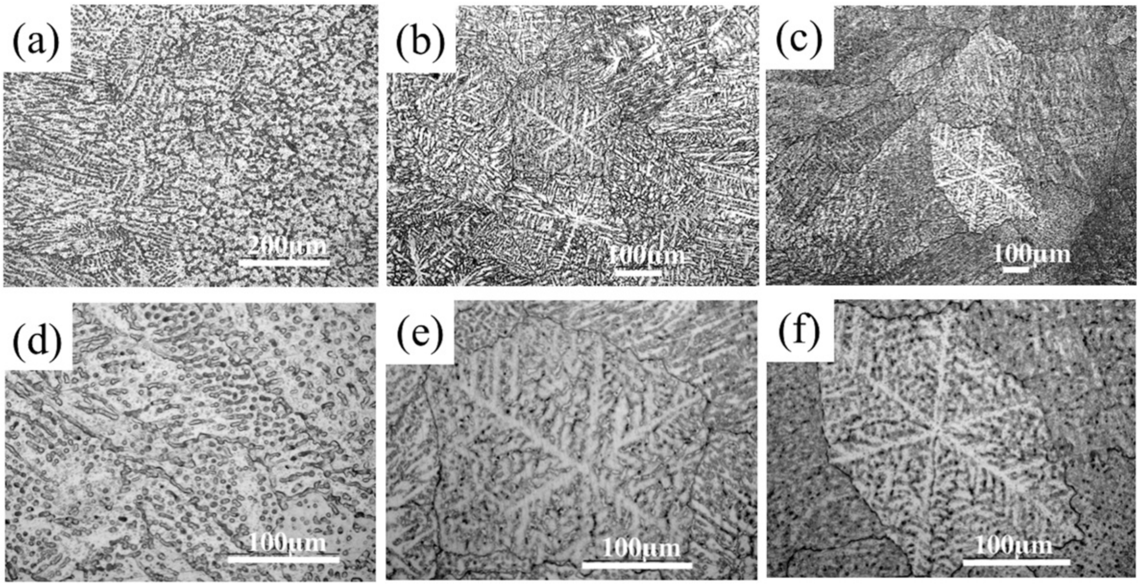

Fig. 3. Microstructure in the FZ after different PWHTs; (a) and (d) are natural ageing, (b) and (e) are T6 ageing, and (c) and (f) are T73 ageing.

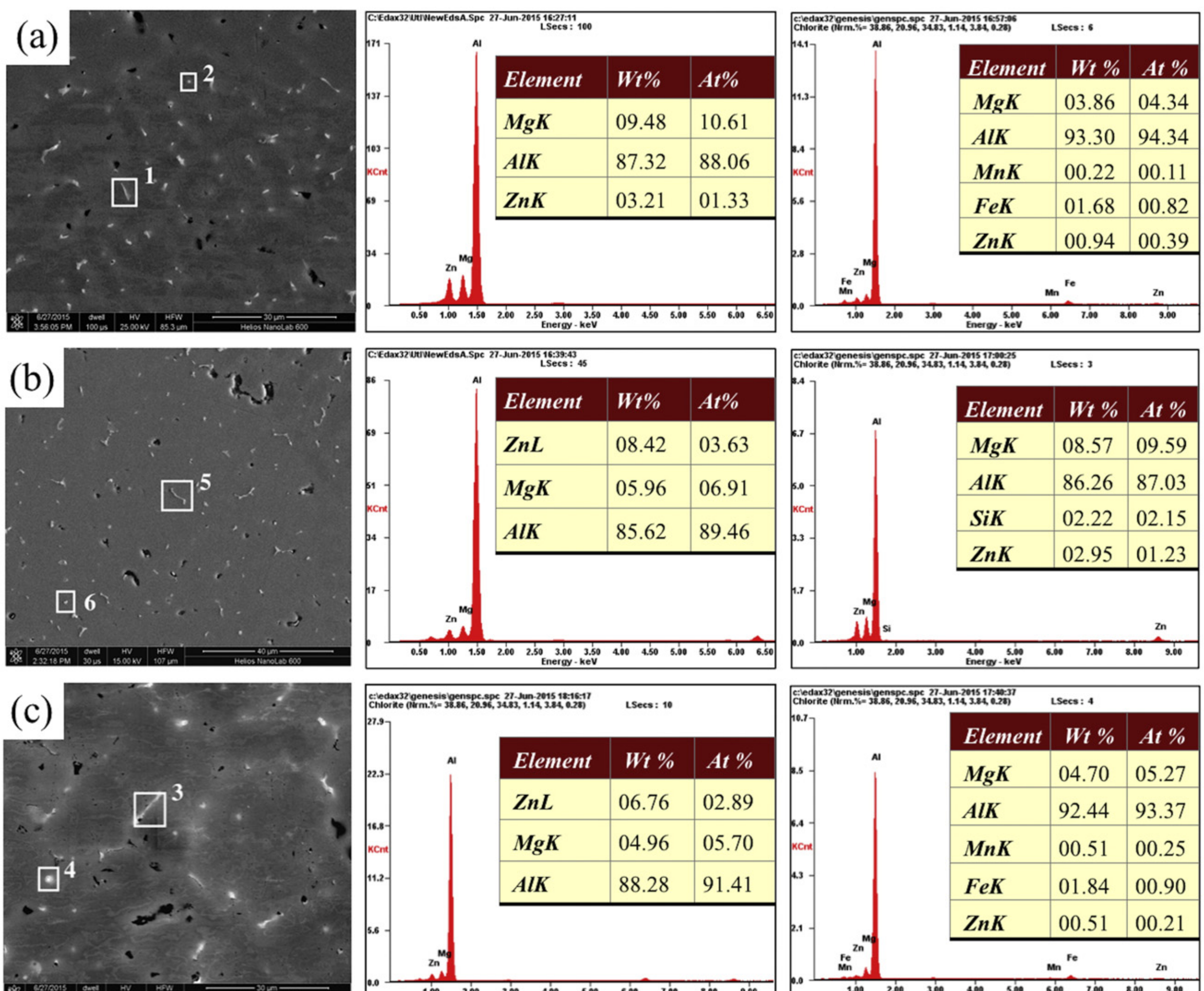

Fig. 4. SEM images of microstructure of fusion zone; (a) NA, (b) T73, and (c) T6.

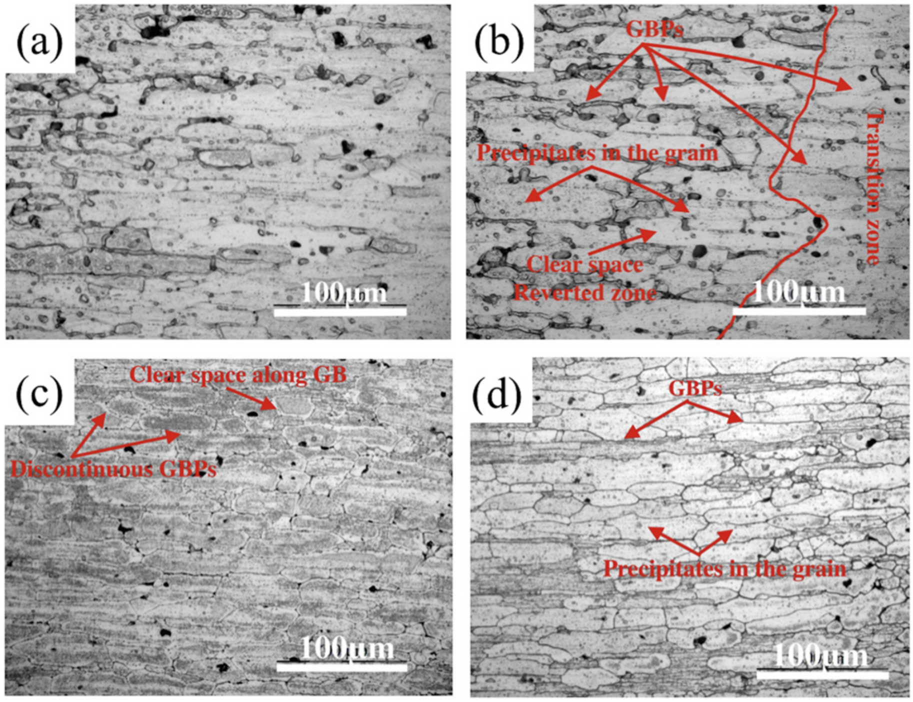

Fig. 5. Microstructure of HAZ; (a) as-weld, (b) NA, (c) T6, and (d) T73.

3.3.2. Morphologies of surface cracks and fracture surface of the SCC sample

After 20 day corrosion, the surfaces of corrosion samples of the BM in NA with apparent corrosion cracks were selected, polished, and then observed by OM and SEM, as shown in Figs. 12 and 13 respectively. SCC can initiate from the tip of pre-cracks (Fig. 12(a)), and then propagate along the GB (Fig. 13(c)). The stress corrosion crack is narrower than the pre-cracks, and becomes even narrower when extending. The SCC propagates stepwise, and some cracks are separated as shown in Fig. 13(a). A mud-like corrosion product and secondary cracks can be found near the main stress corrosion crack (see Fig. 13(b) and (d)). Due to the corrosion attack, some grains and precipitates are dissolved, resulting in corrosion pits around the SCC (Fig. 13(c)). In Figs. 12(a) and 13(a), the SCC is discontinuous. Discontinuous cracks (crack jumps) have also been observed during the formation of SCC in many materials, such as Al alloys [20] and stainless steels [21,22]. As in those findings, jump cracks are usually observed at the tip of main cracks. These jump cracks are described as usually initiating from the main crack, growing separately and finally merging with the main crack [20–22].

After 20 day corrosion, the samples were bent until fractured and the surfaces were observed using OM and SEM. As shown in Fig. 15(a), the typical fractured surface formed in the experiment consisted of four parts: (1) a notch section produced by EDM, (2) a fatigue section produced by a pre-cracking procedure, (3) the SCC propagation section, and (4) a plastic fracture section. The formation of these four sections is attributed to the experimental procedure, in which a notch was first produced using EDM, followed by pre-cracking, SCC testing, and finally breaking of the sample. Each successive experimental procedure is reflected in the fractured surface of the sample. The section of SCC propagation is obviously different from the other sections. It features a relatively rough fractured surface and rolled-tongue-shaped salient perpendicular to the load direction. Fig. 14 shows macrographs of the SCC fractured surface of the BM, HAZ and FZ in different tempers. In the NA temper, SCC is found on the surface of the BM and HAZ, indicating that both are attacked in the corrosion environment. The crack lengths in the BM and HAZ are different; the former is longer, suggesting that SCC propagates more quickly in the BM than in the HAZ. For the T6 and T73 tempers, no SCC is found in the fractured surface of the BM, HAZ, or FZ. This finding further demonstrates that heat treatment can improve the corrosion resistance of hybrid laser-MIG welded Al–Zn–Mg alloy joints.

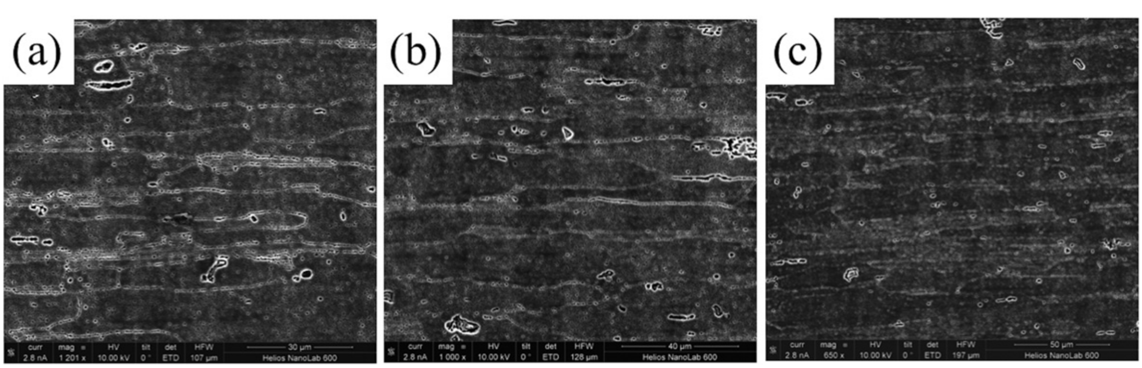

Fig. 6. SEM images of BM; (a) NA, (b) T6, and (c) T73.

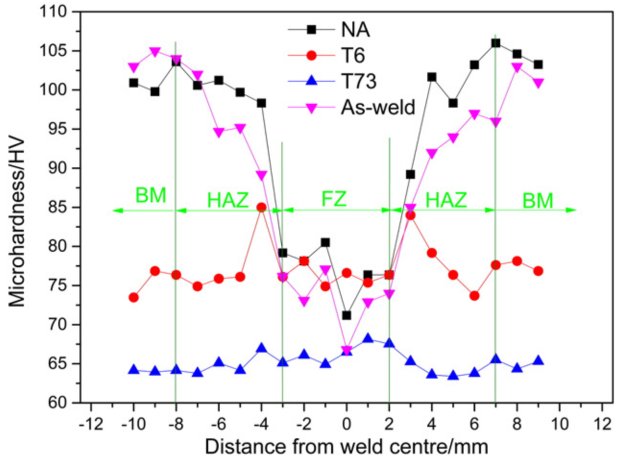

Fig. 7. Microhardness of the welded joint after different PWHTs.

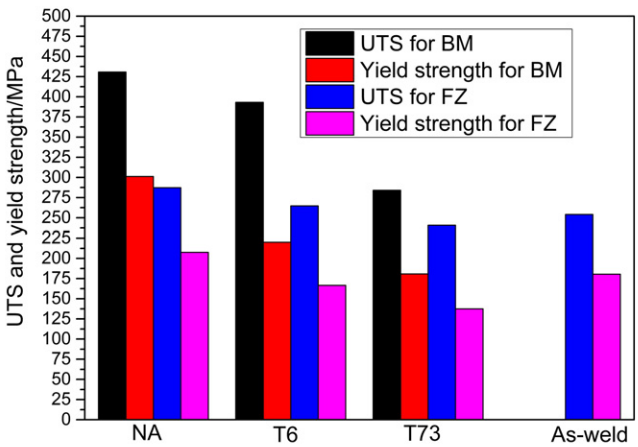

Fig. 8. Ultimate tensile strength and yield strength of the welded joint and BM after different PWHTs.

Detailed SEM images of a fractured surface of the BM in NA are shown in Fig. 15. Fig. 15(b) shows the plastic fracture section of the surface, in which fine dimples can be found, indicating that ductile fracture occurs in this section. In the SCC propagation section, however (Fig. 15(d) and (e)), a crystallized-sugar shaped pattern can be observed in the stress corrosion cracks, which is the sign of intergranular brittle fracture. On the fractured surface of the SCC propagation section, shown in Fig. 15(c), discontinuous SCC can also be observed. Fig. 15(d) further shows the SCC propagating from the pre-cracks, and then extending along the grain boundaries. A mud-like corrosion product is found close to the interface between the pre-crack section and the SCC section (Fig. 16). Energy Dispersive Spectrometer (EDS) was used to test the chemical composition of that product. The result showed that Al and O were the dominant elements, indicating that the corrosion product was probably Al_2O_3.

3.3.3. Results for SCC propagation rate

The SCC propagation rate was measured according to GBT15970.6-2007 and the results are shown in Table 3. The HAZ-0 sample was not pre-cracked. After 20 day corrosion, corrosion attack was found close to the notch, but no SCC propagation was observed. Therefore the rate of SCC propagation was considered to be zero for this sample. The results show that the rate of SCC propagation in the FZ in all tempers was zero, indicating that the FZ was most corrosion-resistant. In the HAZ, crack propagation could only be observed in samples in NA temper, and the average $\Delta a/\Delta t$ in the HAZ is 1.7375×10^{-3} mm/h. As in the HAZ, the BM in NA temper was most susceptible to SCC. The average $\Delta a/\Delta t$ of BM was 3.1597×10^{-3} mm/h, almost twice that in the HAZ. From the results of the SCC propagation rate, it can be seen that the heat treatment improved the SCC resistance of the welded joints.

4. Discussion

4.1. Effect of heat treatment on the strength of the welding joint

The results of microhardness and tensile tests reveal that the strength of the hybrid laser-MIG welded joint of A7N01P-T4 was reduced by the PWHT. This is because the strength of the heat-

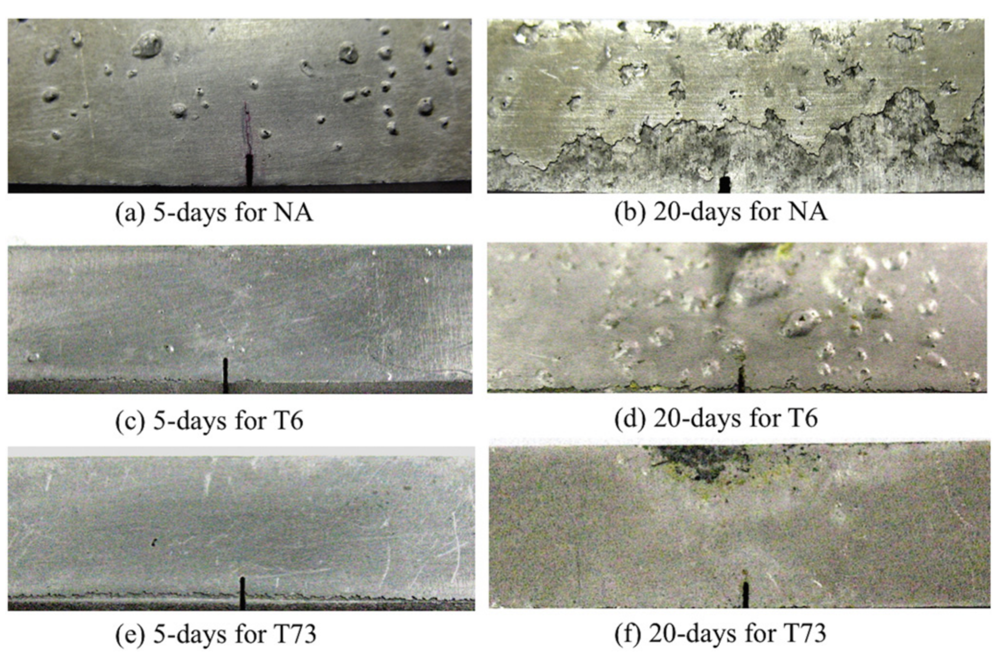

Fig. 9. Macrograph of the BM under different PWHTs after 5 day and 20 day corrosion.

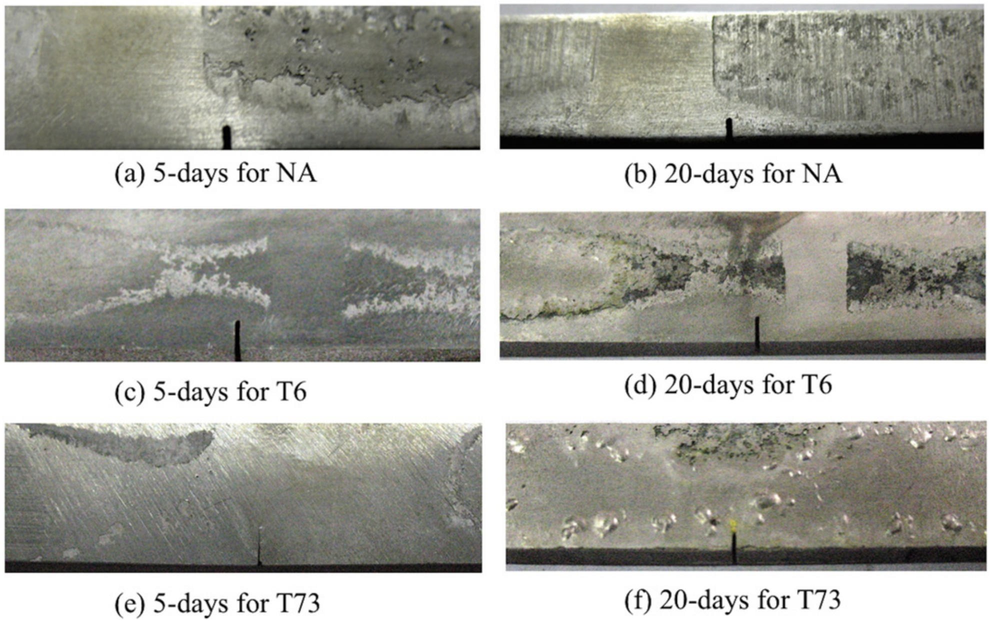

Fig. 10. Macrograph of the HAZ under different PWHTs after 5 day and 20 day corrosion.

treatable alloy depends largely on the precipitates in the alloy [23]. In general, the precipitation sequence of Al–Zn–Mg alloys is [24]:

$\alpha_{sss} \rightarrow \text{GP zone} \rightarrow \text{metastable } \eta\prime \rightarrow \text{stable } \eta$

where α_{sss} is the initial supersaturated solid solution, GP zone is Guinier–Preston zone, η' are metastable precipitates, and η are stable/equilibrium precipitates.

The temper of as-received materials was P-T4, which was first treated by industrial solution and then naturally aged at room temperature. Usually, GP zones and metastable η' phases and stable η with NA could be observed, which determined the strength of the alloys. As shown in Fig. 17(a), the highly dense and fine η' phases are distributed homogeneously within the matrix, and precipitates along the GB are relatively small and distributed continuously. But the GP zones and metastable η' phases are instable when subjected to heat treatment. GP zones and η' precipitates will dissolve in the temperature range of 20–120 °C and 120–250 °C, respectively [25]. Generally, the microstructure will evidence dissolution of GP zones and η' phases when subjected to heat treatment. There are several stages for the change of precipitates: rapid dissolution stage, coarsening stage, and constant volume fraction stage. More details can be found in reference [26].

As illustrated in Fig. 17(b), after ageing at 120 °C for 24 H, the density of phases reduces and some large phases along the GB and within the grain are observed. Meanwhile some precipitate-free zones (PFZs) are formed, which affect the damage and fracture properties of the joint. In this heat treatment, GP zones and η' phases would witness dissolution at the temperature of 120 °C, but the larger phases continue to grow in this period, leading to the decrease of precipitate volume fraction. The reduced strength in this temper compared to that in NA can be attributed to the change of precipitate size and distribution, as well as the lower volume fraction of the precipitate.

After two-step ageing, much larger and coarsened η phases are found along the GB and within the grain. The density of phases also

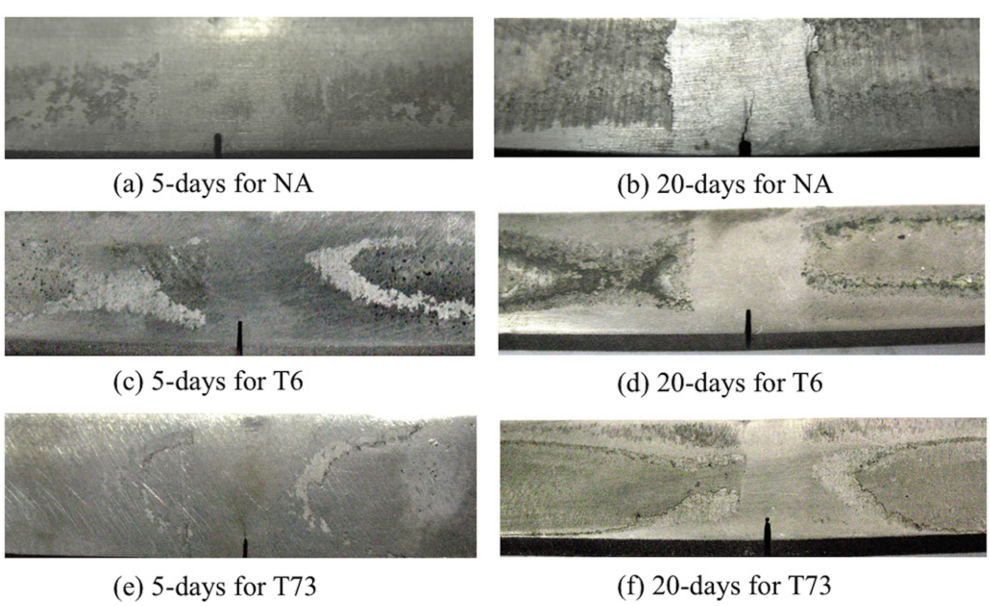

Fig. 11. Macrograph of the FZ under PWHTs after 5 day and 20 day corrosion.

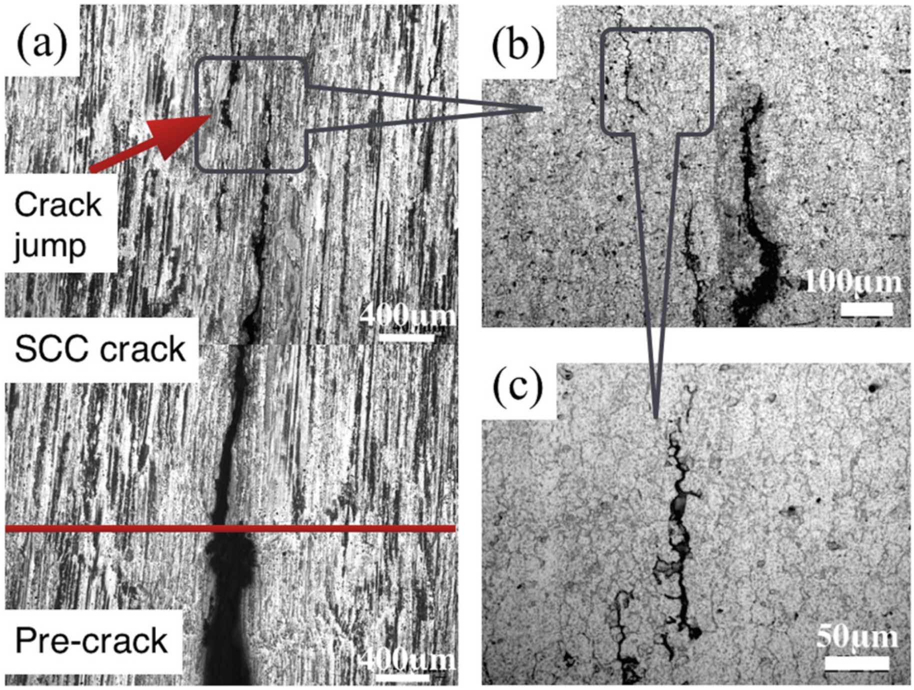

Fig. 12. Morphologies of surface corrosion cracks using OM; (a) overall view of SCC and (b)–(c) enlarged views of some parts of the cracks.

increases compared to that in T6, BM in T73 experienced much higher temperatures. When the ageing temperature increased, the precipitates along the GB would grow, aggregate, and accelerate during the ageing process [27]. Besides, η′ phases and the GP zone would transform into stable η phases with the increasing ageing temperature. Generally, the strength of Al–Zn–Mg alloys is determined by the GP zone and η′ phases. Although stable η phases can be obtained at the higher ageing temperatures, η phases are not incoherent with the matrix and cannot improve the mechanical properties [28]. Therefore, the strength of the BM and the welded joint in T73 temper continues to reduce.

4.2. Effect of heat treatment on the corrosion behaviour of the welded joint

As illustrated in Fig. 17, numerous fine precipitates can be found within and along GB in the NA temper. In the T6 state, the precipitates are characterised by decreasing density, coarseness, and discontinuous distribution. Also, PFZ is formed. In the T73 temper the precipitates are coarser.

Although there is no consensus on the mechanism for SCC of 7XXX aluminium alloys, anodic dissolution theory and hydrogen induced cracking (HIC) are considered as the two main mechanisms for SCC of

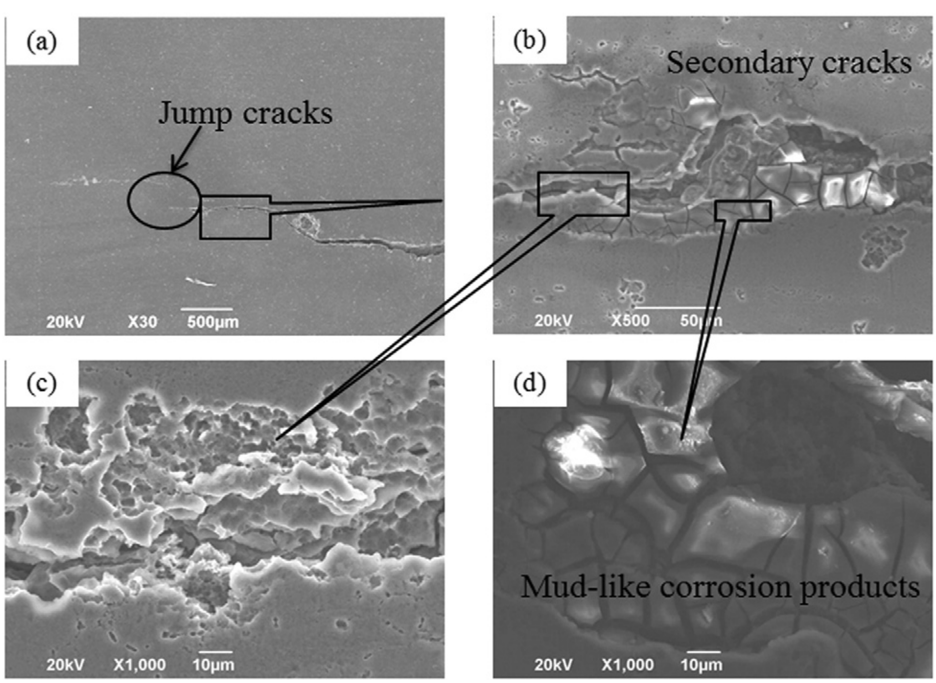

Fig. 13. SEM images of surface corrosion cracks; (a) overall view and (b)–(d) enlarged view of some parts of the cracks.

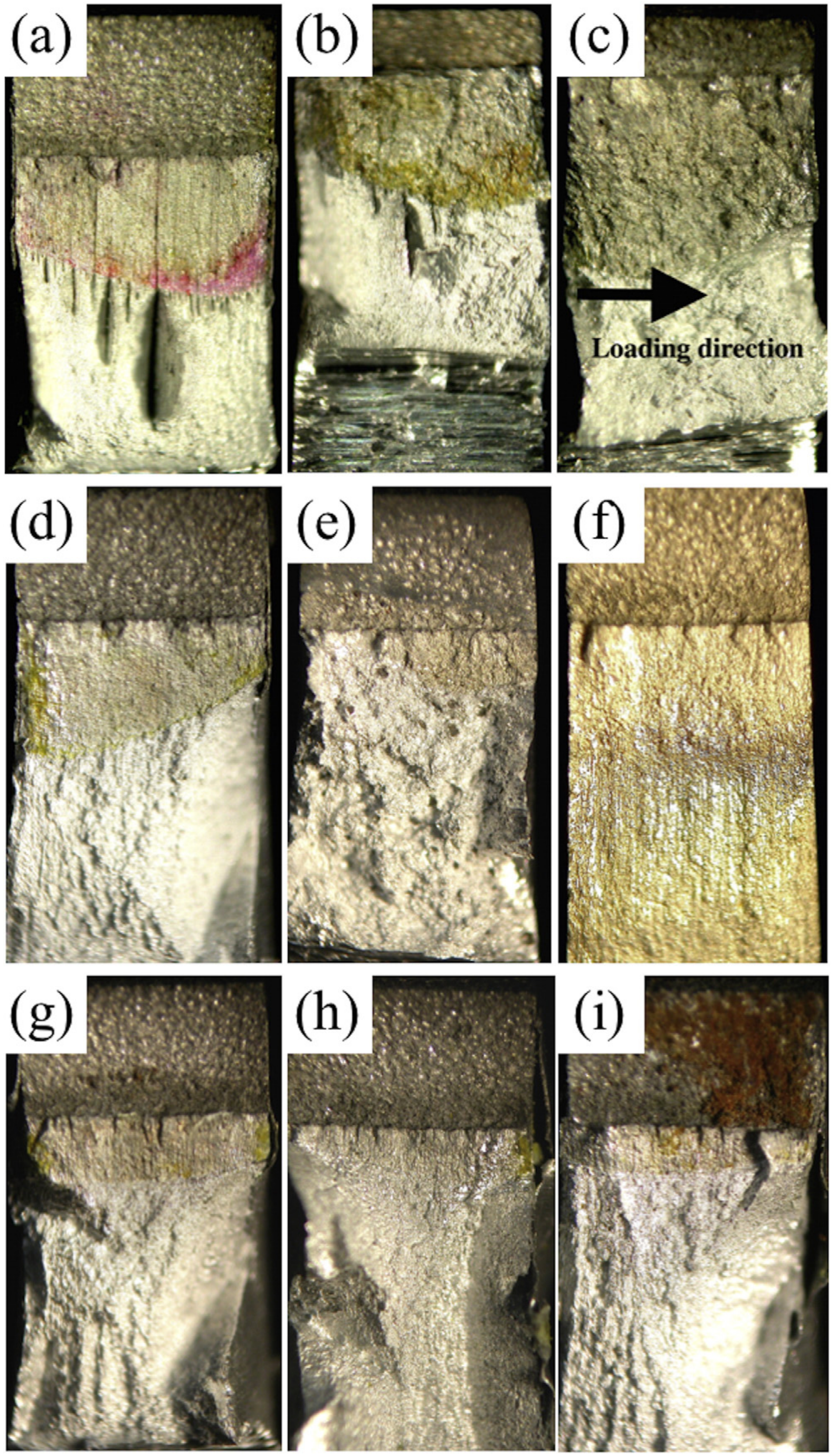

Fig. 14. Macrographs of SCC fractured surface in the BM, HAZ, and FZ at different tempers. (a)–(c) BM, HAZ and FZ in NA; (d)–(f) BM, HAZ and FZ in T6; (g)–(i) BM, HAZ and FZ in T73.

aluminium alloys [13,28]. With the anodic dissolution mechanism, SCC is dependent on the dissolution of anodic phases. In general, it is accepted that the $MgZn_2$ phases at the GB act as an anodic phase and the solution or the oxide as the cathode. The self-corrosion potential of $MgZn_2$ is −1044.7 mV, so it tends to be corroded in a corrosive/moist environment [29]. Therefore, the characteristics of GBPs, which include

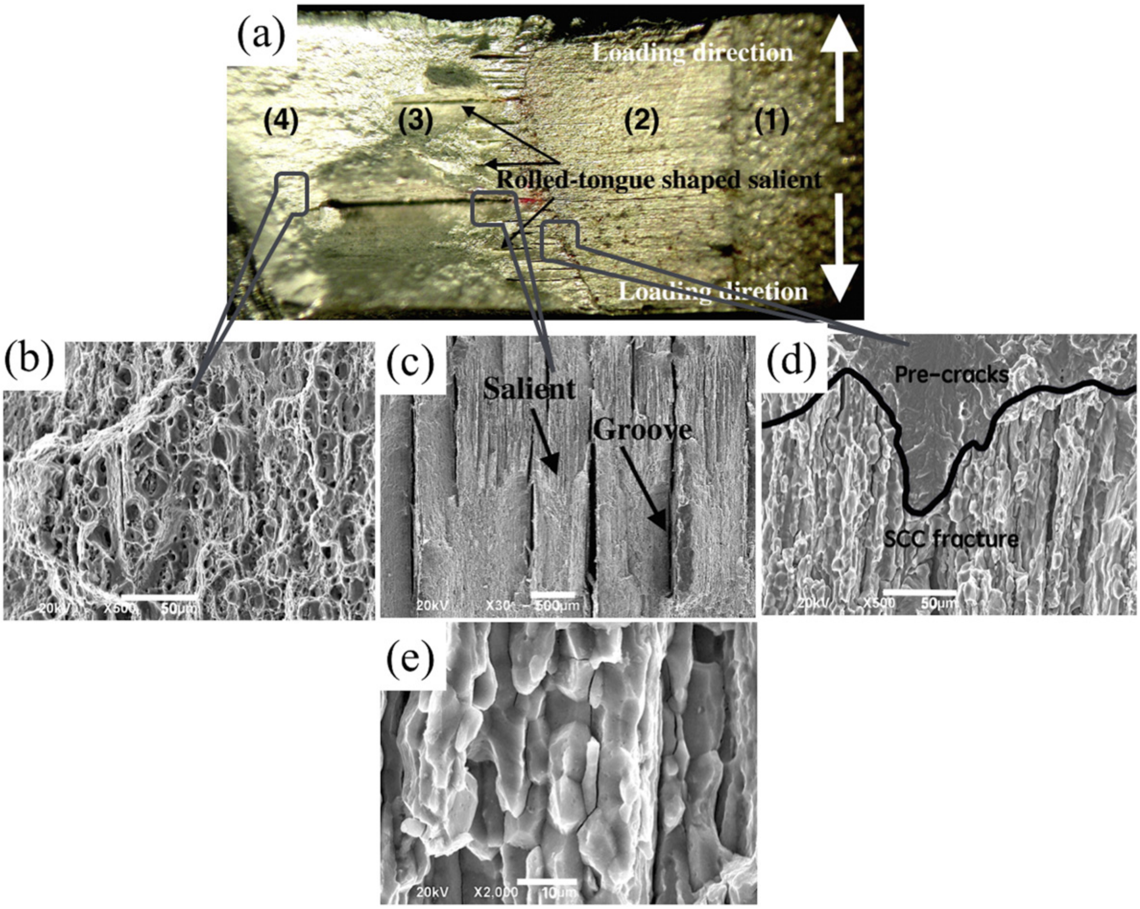

Fig. 15. SEM images of the fractured surface of SCC samples; (a) overall view of the fractured surface, (b) ductile fracture area, (c) SCC propagation area, (d) interface between pre-cracks and SCC propagation areas, and (e) enlarged view of SCC propagation area.

their size, interspace, and content (such as Cu and Mg), determine the corrosion behaviour of Al–Zn–Mg alloys. The dissolution rate can be slowed down with large sized and more widely interspaced GBPs. For the present case, in NA, tiny and more narrowly interspaced precipitates are continuously distributed in the GB, resulting in continuous dissolution of these anodic phases and finally intergranular fracture. However, the size and interspace of GBPs in T6 and T73 are larger, so a lower dissolution rate of GBPs and slower propagation rate can be expected.

In the HIC mechanism, there is a critical or threshold value of the concentration of hydrogen at the tip of the crack at which brittle facture occurs [30]. There is still no consensus as to explanation models for the HE mechanism. Some authors argue that the precipitates within the matrix play an important role in determining susceptibility to HE [30], while another suggests that it is the GBPs that play the dominant role in the HE intergranular fracture [31]. In the first argument, the transport of hydrogen by dislocation movement is determined by the dislocation slip mode, which includes inhomogeneous and homogeneous modes. Generally, inhomogeneous slip mode is more favoured for delivering hydrogen than homogeneous mode does [32]. Increasing phase size can lead to a decrease in slip line spacing and to homogeneous slip character, resulting in better HE resistance [30]. It is reasonable, therefore, that the SCC resistance of welded joint is improved by PWHT because the phase size enlarges after PWHT. In the second argument, large GBPs can trap hydrogen and thus control the concentration of hydrogen in the lattice under the critical/threshold value, arresting the initiating and propagating of SCC cracks [33]. Compared with the NA temper, GBPs in T6 and T73 are larger and more discontinuous, and thus it would take longer for the concentration of lattice hydrogen to reach the critical value. This is why the BM and HAZ in NA have been already attacked by SCC whereas those two regions in T6 and T73 still have no sign of SCCs. In addition, the chemical composition in GB may play an important role. The famous explanation for this is the Mg–H complex model [34], which states that (a) Mg and H can decrease GB strength, although H embrittles the GB more severely than Mg does [35]; (b) Mg serves a dual function — facilitating hydrogen entry and facilitating accumulation and saturation when present as free Mg along the GB, thus leading to HE along the GB [36]. In the case of this study, the temperature increases in the order NA < T6 < T73, resulting in a decrease of Mg segregation in the GB [35,36]. Therefore, the entry accumulation of hydrogen in the GB tends to decrease; the susceptibility to SCCs consequently also decreases.

4.3. Comparison of the corrosion behaviour between different zones of the welded joint

As expected, regardless of the temper of the welded joint, no sign of SCC is found in the FZ. Also, the longer the duration of corrosion, the brighter the FZ is, as verified in Fig. 11. The filling material in the FZ is ER5356, an alloy of the Al–Mg series, whereas the HAZ is an Al–Zn–Mg alloy. According to [37], the electropotential of 5xxx serials Al and 7xxx serials Al is −0.85 V and −0.96 V, respectively. Thus, there is galvanic corrosion happening between these two zones with HAZ acting as anodic member while FZ as cathodic member. That means the HAZ is dissolved while the FZ is protected. Over time, the HAZ darkens due to corrosion while the FZ is relatively brighter. Therefore, the FZ is the safest in the whole joint compared to other two zones, as it was also found that the BM is much more susceptible than the HAZ to SCC, according to the results of the SCC rate and observation of the fracture surface of SCC testing samples.

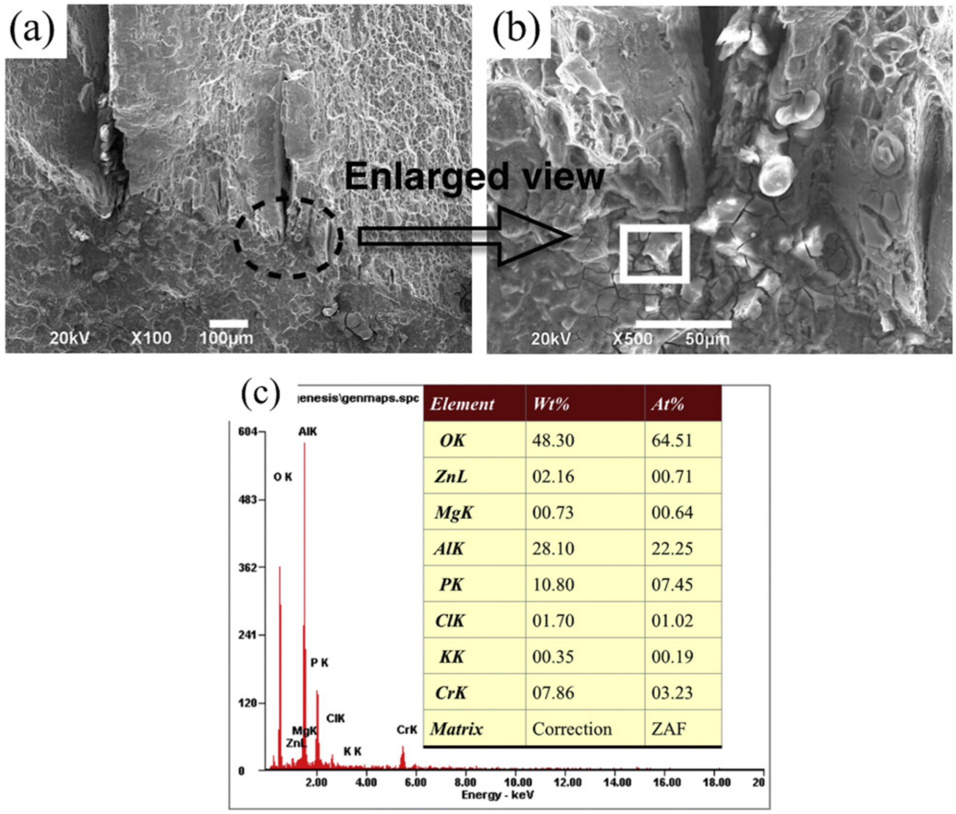

Fig. 16. Interface between the pre-cracks and SCC sections; (a) overall view, (b) enlarged view, and (c) EDS results for mud-like corrosion product.

The most interesting finding in this study is that the BM exhibits poorer SCC resistance than the HAZ, which differs from previous studies in which the weakest part of the welded joint of Al–Zn–Mg alloys was the white zone [10,38], a zone close to the fusion line in the HAZ. That is, the most dangerous part of the welded joint is the HAZ. The welding method used in those previous papers was MIG welding, and the corrosion test method was a slow strain rate test. Those two factors can be considered as the main reasons for the differences between previous results and the present results. The detailed reasons for the difference from these two aspects are discussed below.

Table 3
Results of SCC propagation for the BM, HAZ and FZ in different tempers.

Temper	Sample no.	a (mm)	Δa/Δt (mm/h)
	BM-1	1.556448	3.2426×10^{-3}
	BM-2	1.527504	3.1823×10^{-3}
	BM-3	1.465968	3.0541×10^{-3}
	FZ-4	0	0
NA	FZ-5	0	0
	FZ-6	0	0
	HAZ-7	0.900000	1.8750×10^{-3}
	HAZ-8	0.767952	1.5999×10^{-3}
	HAZ-0	0	0
	BM-65	0	0
	BM-66	0	0
	BM-67	0	0
T6	FZ-62	0	0
(120 °C/24 h)	FZ-63	0	0
	FZ-64	0	0
	HAZ-612	0	0
	HAZ-613	0	0
	HAZ-614	0	0
	BM-71	0	0
	BM-72	0	0
	BM-73	0	0
T73	FZ-74	0	0
(110 °C/8 h + 177 °C/8 h)	FZ-75	0	0
	FZ-76	0	0
	HAZ-77	0	0
	HAZ-78	0	0
	HAZ-79	0	0

Note: a is the average length of stress corrosion cracks on the fractured surface and Δa/Δt is the average SCC propagation rate.

4.3.1. Influence of welding method

Laser-MIG welding process is different from MIG welding process, the comparison of these two welding process can be found elsewhere [2]. Consequently, the thermal history of the HAZ in these two welding methods is quite different, which may lead to different microstructure, mechanical and corrosion properties. The effect of welding process on corrosion and mechanical properties has been previously investigated. Compared to those with Electron beam welding (EBW) and GTAW, AA2219 joints with FSW displayed best tensile and fatigue properties, which is due to the microstructure of fine grains and uniform distribution of strengthening precipitates in the FSW joints [39]. However, such microstructure in FSWs leaded to poorer corrosion resistance than EBW and GTA welds.

It was also found that FSWs showed lower corrosion resistance than EBW and GTA welds. This is mainly due to the presence of finer grains and more uniform distribution of strengthening precipitates in the weld metal of FSW joints. To investigate whether the welding method affects the corrosion behaviour of welded joint, we also tested the corrosion behaviour of a MIG welded joint using the same corrosion method as that in [40], and the results are shown in Fig. 18. It should be noted that the sample number stands for the difference in the chemical composition of copper contained in the tested Al–Mg–Zn alloys. Although the welding method was changed, the results still show that the rate of SCC in all kinds of BM was greater than that in the HAZ. It seems that the welding process has no influence on the local corrosion behaviour of welded AA7N01 joints.

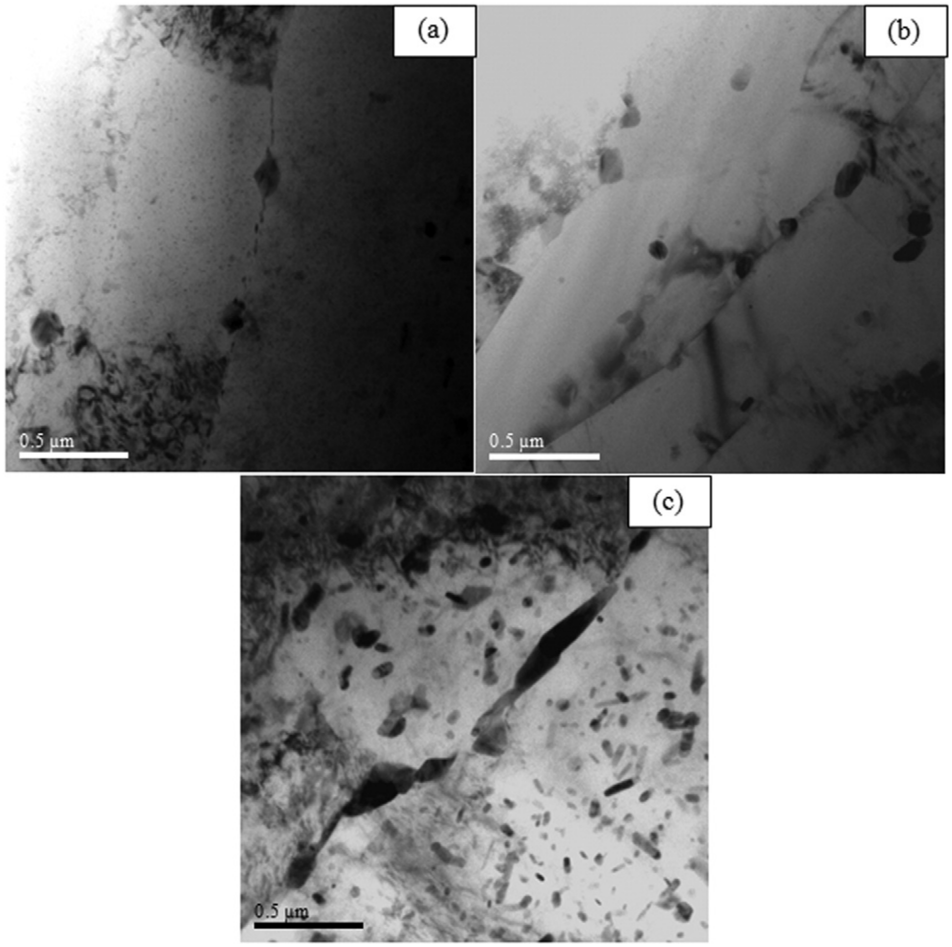

Fig. 17. TEM images of BM in different tempers; (a) NA, (b) T6, and (c) T73.

4.3.2. Influence of corrosion method

The slow strain rate test (SSRT) is a corrosion method used in previous studies. Basically, the specimen consists of all the three parts (BM, HAZ, FZ) in a welded joint. When the sample is loaded, the most stress-concentrated area is the white zone due to the microstructural difference between the HAZ and FZ. Furthermore, the corrosion potential of the HAZ is more positive than that of the FZ, which causes galvanic corrosion. Thus, it is expected the sample would fracture at the white zone. In the method used in the present case, however, pre-cracks that can lead to local stress concentrations are inserted in each zone before corrosion. This method is more likely to measure the local corrosion properties of the welded joint, but the SSRT tests the corrosion resistance of the whole welded joint. The stress concentration caused by pre-cracks is greater than that caused by microstructural differences. Therefore, the SCC will initiate and propagate from the pre-cracks, an assumption that is also verified in Figs. 12 and 15, and the microstructure near the pre-crack will govern the corrosion behaviour.

The microstructure in the HAZ is heterogeneous due to the non-isothermal history during welding. Basically, the HAZ can be further divided into three zones [25]: (a) a fully reverted zone in which all precipitates have dissolved during the high-temperature stage and where some GP zones can re-precipitate during the low-temperature stage, (b) a transition zone characterised by the partial dissolution of initially present precipitates with some coarsening in the region of highest temperatures, and (c) the unaffected material. The pre-cracks in the HAZ are probably located in the transition zone, where the phase size is coarser than that in the BM and the number of density phases is reduced. As illustrated in Fig. 5, large and discontinuous precipitates can be found along the GB, which is similar to the microstructure of the BM in T6 or T73. According to the analysis in Section 4.2, this kind of microstructure is beneficial to SCC resistance, so it is reasonable for the HAZ to display better SCC resistance than the BM in NA.

5. Conclusion

In this paper the SCC behaviour of different zones in a hybrid laser-MIG welded joint is studied using pre-cracked bending samples treated with 3.5% NaCl solution. The effect of PWHT on the corrosion behaviour

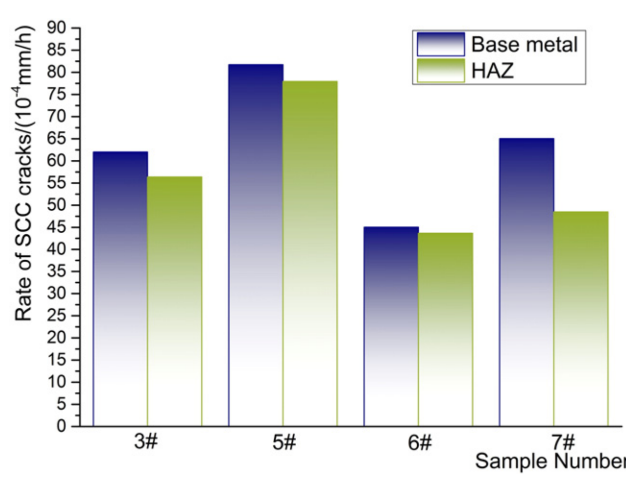

Fig. 18. Rate of SCC propagation for MIG welded AA7N01.

of the hybrid welded joint is also investigated. The following conclusions are drawn:

(1) The order sequence of SCC resistance for different part of hybrid laser-MIG welding A7N01 joints is: FZ > HAZ > BM;
(2) PWHT changes the precipitates from coherent η′ and GP to incoherent η, resulting in reduction of strength of the hybrid welded joint;
(3) Larger and coarsened precipitates discontinuously distribute along the GB due to PWHT, leading to improvement of SCC resistance of the hybrid welded joint;
(4) In NA, the BM is more prone than the HAZ to SCC, because the microstructure of the HAZ, more specifically in the transition zone of the HAZ, becomes more resistant to SCC due to the non-isothermal history during hybrid laser-MIG welding.

Acknowledgement

The authors gratefully acknowledge the financial support from the National Key Technology R&D Program of China (No. 2009BAG12A07-B03), the Chinese Scholarship Council (CSC), and ARC's linkage project programme (No. LP130101001). We also thank Xiaoli Che, Yirong Wang, Zongtao Zhu and Yi Xiao for their helpful discussion and useful comments.

This work was performed in part at the ACT node of Australia National Fabrication Facility.

References

[1] S. Yan, Y. Nie, Z. Zhu, H. Chen, G. Gou, J. Yu, G. Wang, Characteristics of microstructure and fatigue resistance of hybrid fiber laser-MIG welded Al–Mg alloy joints, Appl. Surf. Sci. 298 (2014) 12–18.
[2] S. Yan, H. Chen, Z. Zhu, G. Gou, Hybrid laser-metal inert gas welding of Al–Mg–Si alloy joints: microstructure and mechanical properties, Mater. Des. 61 (2014) 160–167.
[3] S.C. Wu, XY, R.Z. Zuo, W.H. Zhang, H.L. Xie, J.Z. Jiang, Porosity, element loss, and strength model on softening behavior of hybrid laser arc welded Al–Zn–Mg–Cu alloy with synchrotron radiation analysis, Weld. J. 92 (2013) 8.
[4] W.M. Steen, Arc augmented laser processing of materials, J. Appl. Phys. 51 (1980) 5636.
[5] P. Leo, G. Renna, G. Casalino, A.G. Olabi, Effect of power distribution on the weld quality during hybrid laser welding of an Al–Mg alloy, Opt. Laser Technol. 73 (2015) 118–126.
[6] G. Casalino, M. Mortello, P. Leo, K.Y. Benyounis, A.G. Olabi, Study on arc and laser powers in the hybrid welding of AA5754 Al-alloy, Mater. Des. 61 (2014) 191–198.
[7] M. Mazar Atabaki, J. Ma, W. Liu, R. Kovacevic, Pore formation and its mitigation during hybrid laser/arc welding of advanced high strength steel, Mater. Des. 67 (2015) 509–521.
[8] C. He, C. Huang, Y. Liu, J. Li, Q. Wang, Effects of mechanical heterogeneity on the tensile and fatigue behaviours in a laser-arc hybrid welded aluminium alloy joint, Mater. Des. 65 (2015) 289–296.
[9] R.A. Kelsey, Effect of heat input on welds in aluminum alloy 7039, Weld. Res. Suppl. 12 (1971) 507–514.
[10] M.C. Reboul, BD, M. Lashermes, The stress corrosion susceptibility of aluminum alloy 7020 welded sheets, Corros. Sci. 25 (1985) 999–1018.
[11] Y.E. Wu, Y.T. Wang, Enhanced SCC resistance of AA7005 welds with appropriate filler metal and post-welding heat treatment, Theor. Appl. Fract. Mech. 54 (2010) 19–26.
[12] S.P. Knight, N. Birbilis, B.C. Muddle, A.R. Trueman, S.P. Lynch, Correlations between intergranular stress corrosion cracking, grain-boundary microchemistry, and grain-boundary electrochemistry for Al–Zn–Mg–Cu alloys, Corros. Sci. 52 (2010) 4073–4080.
[13] X.Y. Sun, B. Zhang, H.Q. Lin, Y. Zhou, L. Sun, J.Q. Wang, Correlations between stress corrosion cracking susceptibility and grain boundary microstructures for an Al–Zn–Mg alloy, Corros. Sci. 77 (2013) 103–112.
[14] V. Fahimpour, S.K. Sadrnezhaad, F. Karimzadeh, Corrosion behavior of aluminum 6061 alloy joined by friction stir welding and gas tungsten arc welding methods, Mater. Des. 39 (2012) 329–333.
[15] H. Wensheng, E.I. Meletis, Mater. Sci. Forum 331 (2000) 1683–1688.
[16] ASTM B557-10, Standard Test Methods for Tension Testing Wrought and Cast Aluminum and Magnesium-alloy Products, American Society of Testing Materials, 2010.
[17] GB 15970.6-2007. National Standard of China. Corrosion of metals and alloys—stress corrosion testing—part 6: preparation and use of pre-cracked specimens for tests under constant load or constant displacement.
[18] A.D. Zervaki, Computational kinetics simulation of the dissolution and coarsening in the HAZ during laser welding of 6061-T6 Al-alloy, Weld. J. Res. Suppl. 86 (2007) 211s–220s.
[19] T. Marlaud, B. Malki, A. Deschamps, B. Baroux, Electrochemical aspects of exfoliation corrosion of aluminium alloys: the effects of heat treatment, Corros. Sci. 53 (2011) 1394–1400.
[20] J. Zhang, S. Kalnaus, M. Behrooz, Y. Jiang, Effect of loading history on stress corrosion cracking of 7075-T651 aluminum alloy in saline aqueous environment, Metall. Mater. Trans. A 42 (2010) 448–460.
[21] H. Masuda, SKFM observation of SCC on SUS304 stainless steel, Corros. Sci. 49 (2007) 120–129.
[22] L.J. Qiao, K.W. Gao, A.A. Volinsky, X.Y. Li, Discontinuous surface cracks during stress corrosion cracking of stainless steel single crystal, Corros. Sci. 53 (2011) 3509–3514.
[23] T. Ma, GdO, Softening behaviour of Al–Zn–Mg alloys due to welding, Mater. Sci. Eng. A 266 (1999) 198–204.
[24] D.K. Xu, N. Birbilis, P.A. Rometsch, The effect of pre-ageing temperature and retrogression heating rate on the strength and corrosion behaviour of AA7150, Corros. Sci. 54 (2012) 17–25.
[25] M. Nicolas, A. Deschamps, Characterisation and modelling of precipitate evolution in an Al–Zn–Mg alloy during non-isothermal heat treatments, Acta Mater. 51 (2003) 6077–6094.
[26] T. Marlaud, A. Deschamps, F. Bley, W. Lefebvre, B. Baroux, Evolution of precipitate microstructures during the retrogression and re-ageing heat treatment of an Al–Zn–Mg–Cu alloy, Acta Mater. 58 (2010) 4814–4826.
[27] C. Li, Q. Pan, Y. Shi, Y. Wang, B. Li, Influence of aging temperature on corrosion behavior of Al–Zn–Mg–Sc–Zr alloy, Mater. Des. 55 (2014) 551–559.
[28] Y. Shi, Q. Pan, M. Li, X. Huang, B. Li, Influence of alloyed Sc and Zr, and heat treatment on microstructures and stress corrosion cracking of Al–Zn–Mg–Cu alloys, Mater. Sci. Eng. A 621 (2015) 173–181.
[29] J.K. Park, AJA, Microchemical analysis of precipitate free zones in 7075-Al in the T6, T7 and RRA tempers, Acta Metall. 39 (1991) 591–598.
[30] D. Nguyen, AWT, I.M. Bernstein, Microstructural effects on hydrogen embrittlement in a high purity 7075 aluminum alloy, Acta Metall. 35 (1987) 2417–2425.
[31] G.M. Pressouyre, IMB, An example of the effect of hydrogen trapping on hydrogen embrittlement, Metall. Trans. A. 12 (1981) 835.
[32] J.K. Park, AJA, Effect of retrogression and reaging treatments on the microstructure of Al-7075-T651, Metall. Mater. Trans. A 15 (1984) 1531–1543.
[33] M. Puiggali, AZ, J.M. Olive, E. Renauld, D. Desjardins, M. Cid, Effect of microstructure on stress corrosion cracking of an Al–Zn–Mg–Cu alloy, Corros. Sci. 40 (1998) 805–819.
[34] X.Y. Sun, B. Zhang, H.Q. Lin, Y. Zhou, L. Sun, J.Q. Wang, E.H. Han, W. Ke, Atom probe tomographic study of elemental segregation at grain boundaries for a peak-aged Al–Zn–Mg alloy, Corros. Sci. 79 (2014) 1–4.
[35] R.G. Song, W. Dietzel, B.J. Zhang, W.J. Liu, M.K. Tseng, A. Atrens, Stress corrosion cracking and hydrogen embrittlement of an Al–Zn–Mg–Cu alloy, Acta Mater. 52 (2004) 4727–4743.
[36] R.K. Viswanadham, TSS, J.A. Green, Grain boundary segregation in Al–Zn–Mg alloys—implications to stress corrosion cracking, Metall. Trans. A 11 (1980) 85–89.
[37] J.R. Davis, Corrosion of Aluminum and Aluminum Alloys, ASM International, 1999 28.
[38] C. Garca-Cordovilla, EL, A. Pamies, Microstructure and susceptibility to stress corrosion cracking of Al–Zn–Mg weldments (AA-7017), Mater. Sci. Eng. A 174 (1994) 173–186.
[39] S. Malarvizhi, V. Balasubramanian, Effect of welding processes on AA2219 aluminium alloy joint properties, Trans. Nonferrous Metals Soc. China 21 (2011) 962–973.
[40] Y.-L. Zhou, The Effects of Alloying Elements on the A7N01S-T5 Aluminium Alloy and its Welded Joints of High-speed Train[D], Southwest Jiaotong Univeristy, 2013.